

Molecular engineering of dispersed tin phthalocyanine on carbon nanotubes for selective CO₂ reduction to formate

Baotong Chen ^{a,1}, Haiyuan Zou ^{c,1}, Lei Gong ^a, Hao Zhang ^a, Ning Li ^a, Houhe Pan ^a, Kang Wang ^{a,*}, Tao Yang ^d, Yunpeng Liu ^{b,*}, Lele Duan ^c, Jiemin Liu ^{a,*}, Jianzhuang Jiang ^{a,*}

^a Beijing Advanced Innovation Center for Materials Genome Engineering, Beijing Key Laboratory for Science and Application of Functional Molecular and Crystalline Materials, Department of Chemistry and Chemical Engineering, School of Chemistry and Biological Engineering, University of Science and Technology Beijing, Beijing 100083, China

^b Institute of High Energy Physics, Chinese Academy of Sciences, Beijing 100049, China

^c Department of Chemistry and Shenzhen Grubbs Institute Southern University of Science and Technology (SUSTech), China

^d Innovation Research Institute for Carbon Neutrality, University of Science and Technology Beijing, Beijing 100083, China



ARTICLE INFO

Keywords:

CO₂ reduction reaction

Tin phthalocyanine

Formate molecular engineering

MEA cell

ABSTRACT

The synthesis of formic acid/formate from CO₂ electrolysis is appealing for the sustainable production of fuels, which however requires highly active and selective electrocatalysts. Herein, supporting a series of phthalocyanine tin (IV) complexes on multi-walled carbon nanotubes (CNTs) generated three composite catalysts, namely SnPc@CNTs, SnPc-8 F@CNTs, and SnPc-8OCH₃ @CNTs. Electrochemical tests indicate the high activity of these three catalysts in particular SnPc-8 F@CNTs towards CO₂-to-formate conversion with a maximal Faraday efficiency (FE) of 91.7% at -1.2 V versus RHE and excellent stability in flow cell, comparable to thus far state-of-the-art catalysts towards CO₂-to-formate conversion. Remarkably, when used as the cathode catalyst in membrane electrode assembly, SnPc-8 F@CNTs stably delivers a current density of 100 mA cm⁻² with a FE_{formate} of 85% at -2.6 V for 200 h. A series of in situ spectroscopy tests and theoretical calculations demonstrate the significant effect of the electron-withdrawing F atoms on improving the catalytic activity of SnPc-8 F@CNTs.

1. Introduction

Electrocatalytic CO₂ reduction reaction (CO₂RR) provides an effective route to convert greenhouse CO₂ into useful carbon feedstocks and value-added chemicals by electrical energy from renewable energy sources [1–7]. The synthesis of formic acid/formate from CO₂ is one of the most economically promising options owing to the wide applications of formic acid/formate in pharmaceuticals, textiles, and tanning industries as well as hydrogen storage and fuel cells [8–14]. Over the past decades, great efforts have been devoted to developing efficient catalysts including Sn [15–17], In [18–20], Bi [21–24], Sb [25], Pd [26–28], and Cu-based [29–31] catalysts for electrocatalytic CO₂ reduction to formic acid/formate. Among these catalysts, Sn-based catalysts such as SnO₂, [32,33] SnO, [34] SnS₂, [35,36] and Sn-based alloy [37,38] attract much attention due to their low toxic and environmentally friendly properties as well as their low cost. However, these Sn-based catalysts still fail to achieve the industry requirements of high

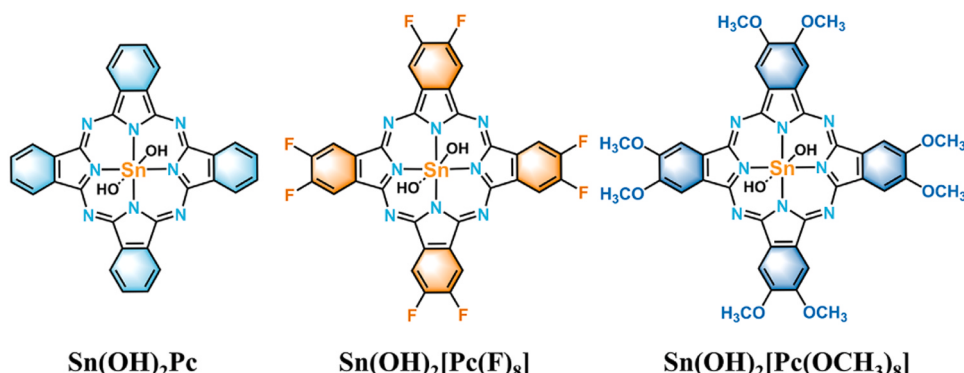
selectivity (> 90%), the high reaction rate (current density > 200 mA cm⁻²), and long-term stability [39,40].

Single atomic site catalysts (SASCs) feature optimal metal utilization, tunable electronic structures, and high activity, emerging as promising catalysts for various reactions including oxygen reduction reaction (ORR) [41–43], hydrogen evolution reaction (HER) [44–46], and CO₂RR. [47–50] In particular, Sn-based SASCs with Sn-N_x as the active sites have exhibited notable selectivity and activity for electrocatalytic CO₂-to-formate conversion [51–53]. In 2019, Xie *et al.* first fabricated single atom Sn^{δ+} on N-doped graphene, which exhibited low onset overpotential of 60 mV for formate production with maximum Faradaic efficiency (FE_{formate}) of 74.3% at -1.6 V versus the standard hydrogen electrode [51]. Subsequently, Zhang and co-workers developed an Sn-SAs/NC catalyst with a maximum FE_{formate} of 88% at -0.75 V versus RHE [52]. Unfortunately, these reported Sn-based SASCs are synthesized through high-temperature pyrolysis, leading to the non-uniform local environment surrounding the active centers and in turn making

* Corresponding authors.

E-mail addresses: kangwang@ustb.edu.cn (K. Wang), liyunpeng@ihep.ac.cn (Y. Liu), liujm@ustb.edu.cn (J. Liu), jianzhuang@ustb.edu.cn (J. Jiang).

¹ These authors contributed equally to this work.



Scheme 1. The molecular structure of $\text{Sn}(\text{OH})_2\text{Pc}$, $\text{Sn}(\text{OH})_2[\text{Pc}(\text{F})_8]$, and $\text{Sn}(\text{OH})_2[\text{Pc}(\text{OCH}_3)_8]$.

it difficult to clearly understand the catalytic mechanism towards rationally improving the catalytic performance. Assembling single-site molecules such as metal phthalocyanines (MPcs) [54–56] and metal porphyrins (MPors) [57–60] on the conductive substrates would be an ideal way to overcome the above issues, owing to the well-defined coordination environment and tailorabile electronic structure of the metal active centers in such molecule-based SASCs. In this respect, Wang and co-workers anchored CoPc molecules on CNTs, showing a high and stable current density of over 10 mA cm^{-2} at -0.52 V versus RHE with a FE of over 90% for CO_2 reduction to CO. This group also demonstrated that introducing the cyano groups to the CoPc molecule can achieve enhanced catalytic performance with FE_{CO} over 95% from -0.53 to -0.63 V versus RHE. [61] Liang *et al.* supported a series of NiPcs with different substituent groups on CNTs and demonstrated the highest activity of NiPc-OMe molecularly dispersed electrocatalysts in catalyzing CO_2 -to-CO conversion with > 99.5% selectivity at a high current density of -300 mA cm^{-2} in a gas diffusion electrode [62]. Despite transition metal phthalocyanines have been widely used to catalyze CO_2RR thus far, the CO_2RR activity of MPC-based SASCs with main group metal elements (e.g. Sn, In, Bi, Sb) as active centers has been rarely explored, limited to only unsubstituted phthalocyanine tin (IV) immobilized on carbon nanotubes with mediocre performance (current density $< 100 \text{ mA cm}^{-2}$) [63,64], to the best of our knowledge.

Herein, supporting a series of phthalocyanine tin (IV) complexes including unsubstituted phthalocyanine tin (IV) $\{\text{Sn}(\text{OH})_2\text{Pc}\}$, 2,3,9,10,16,17,23,24-octafluorophthalocyaninato tin (IV) $\{\text{Sn}(\text{OH})_2[\text{Pc}(\text{F})_8]\}$, and 2,3,9,10,16,17,23,24-octamethoxyphthalocyaninato tin (IV) $\{\text{Sn}(\text{OH})_2[\text{Pc}(\text{OCH}_3)_8]\}$ on multi-walled CNTs through π - π stacking generates three composite catalysts, namely SnPc@CNTs , SnPc-8 F@CNTs , and $\text{SnPc-8OCH}_3 @\text{CNTs}$ (Scheme 1). Electron microscopy and X-ray absorption near-edge structure (XANES) measurements disclose the atomic dispersion of Sn sites coordinated by ~6 N/O atoms in all three catalysts. Electrochemical tests indicate the high activity of SnPc-8 F@CNTs towards CO_2 -to-formate conversion with a maximal Faraday efficiency of 91.7% for formate at -1.2 V versus RHE, a large part current density of formate (J_{formate}) of 600 mA cm^{-2} at -1.5 V versus RHE, and excellent stability in the flow cell, comparable to the thus far state-of-the-art catalysts for formate production from CO_2RR . Remarkably, when used as the cathode catalyst in a zero-gap membrane electrode assembly (MEA), SnPc-8 F@CNTs stably delivers a current density of 100 mA cm^{-2} at a full-cell voltage of -2.6 V for 200 h, indicating its great practical application potential. In situ X-ray absorption spectroscopy (XAS) and in situ attenuated total reflection infrared (ATR-IR) spectroscopy measurements as well as theoretical calculations demonstrate the significant effect of the electron-withdrawing F atoms on improving the catalytic activity of SnPc-8 F@CNTs .

2. Experimental

2.1. General remarks

SnCl_2 , 1,2-dicyanobenzene, 4,5-difluorophthalonitrile, 4,5-dimethoxyphthalonitrile, and 1,8-diazabicyclo [5.4.0] undec-7-ene were purchased from Alfa Aesar. amyl alcohol, methanol, N, N-Dimethylformamide (DMF) was purchased from Sinopharm Chemical Reagent Co., Ltd (China). Carbon nanotubes (CNTs) were purchased from XFNANO Co., Ltd(China). All the reagents were used without further purification.

2.2. Synthesis of $\text{Sn}(\text{OH})_2[\text{Pc}(\text{F})_8]$

4,5-Difluorophthalonitrile (100 mg) and SnCl_2 (189.6 mg) were added to a Schlenk flask equipped with a stir bar. After several cycles of vacuum and refiling with nitrogen, amyl alcohol (3 mL) and 1,8-diazabicyclo [5.4.0] undec-7-ene (0.6 mL) were added. The reaction mixture was then heated to 145°C and kept for 6 h. After being cooled to room temperature, the volatiles were removed under reduced pressure. The crude product was washed with methanol and then extracted via a Soxhlet apparatus with DMF for two days and dried in a vacuum to give the product $\text{Sn}(\text{OH})_2[\text{Pc}(\text{F})_8]$ (42 mg).

2.3. Synthesis of $\text{Sn}(\text{OH})_2\text{Pc}$

Using the synthesis procedure for $\text{Sn}(\text{OH})_2\text{Pc}$ with 1,2-dicyanobenzene (100 mg) instead of 4,5-difluorophthalonitrile (100 mg) as starting material, $\text{Sn}(\text{OH})_2\text{Pc}$ (50 mg) was obtained.

2.4. Synthesis of $\text{Sn}(\text{OH})_2[\text{Pc}(\text{OCH}_3)_8]$

By means of the synthesis procedure for $\text{Sn}(\text{OH})_2[\text{Pc}(\text{OCH}_3)_8]$ with 4,5-dimethoxyphthalonitrile (100 mg) instead of 4,5-difluorophthalonitrile (100 mg) as starting material, $\text{Sn}(\text{OH})_2[\text{Pc}(\text{OCH}_3)_8]$ (36 mg) was obtained.

2.5. Synthesis of SnPc-8 F@CNTs

30 mg CNTs were dispersed in 30 mL of DMF by sonication for 1 h. Then, $\text{Sn}(\text{OH})_2[\text{Pc}(\text{F})_8]$ (2 mg) dissolved in DMF (30 mL) was added into the CNTs suspension. The mixture was sonicated for another 1 h and stirred at room temperature for 24 h. Then, the mixture was centrifuged and the precipitate was washed with DMF and ethanol. Finally, the precipitate was lyophilized, giving SnPc-8 F@CNTs (26 mg).

2.6. Synthesis of SnPc@CNTs

By means of the synthesis procedure for SnPc-8 F@CNTs with Sn

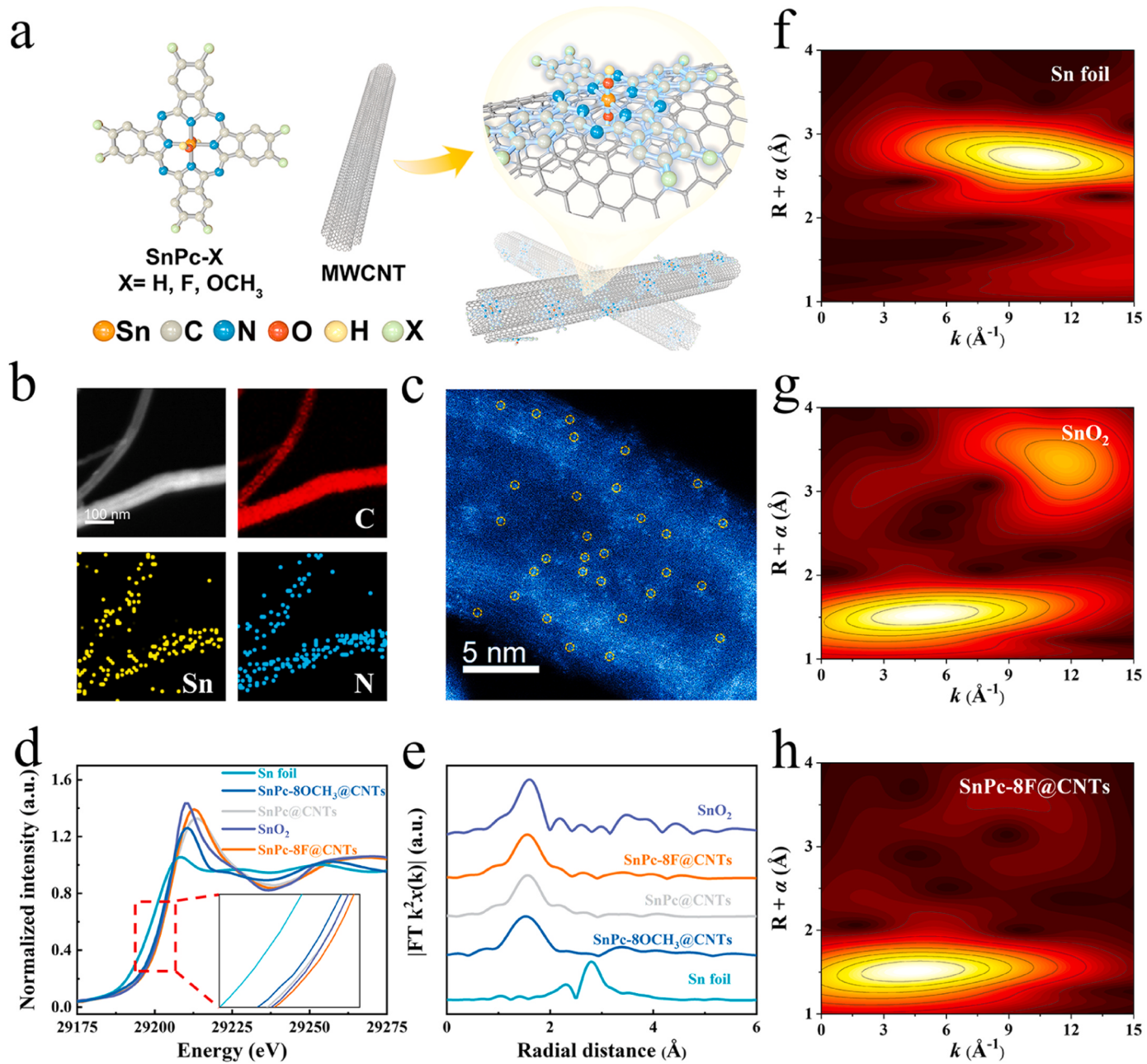


Fig. 1. (a) A schematic presentation of the SnPc molecules anchored on the side walls of CNTs. (b) EDS elemental mappings and (c) AC-HAAD-STEM images of SnPc-8 F@CNTs. (d) Sn K-edge XANES and (d) FT-EXAFS spectra of Sn foil, SnO₂, SnPc@CNTs, SnPc-8 F@CNTs, and SnPc-8OCH₃ @CNTs. WT plots for the Sn K-edge EXAFS of (f) Sn foil, (g) SnO₂, and (h) SnPc-8 F@CNTs.

(OH)₂Pc (1.8 mg) instead of Sn(OH)₂[Pc(F)₈] (2 mg) as starting material, SnPc@CNTs (24 mg) was obtained.

2.7. Synthesis of SnPc-8OCH₃ @CNTs

By means of the synthesis procedure for SnPc-8 F@CNTs with Sn(OH)₂[Pc(OCH₃)₈] (2.2 mg) instead of Sn(OH)₂[Pc(F)₈] (2 mg) as starting material, SnPc-8OCH₃ @CNTs (25 mg) was obtained.

3. Results and discussion

3.1. Materials synthesis and characterization

Fig. 1a illustrates the synthesis of SnPc@CNTs, SnPc-8 F@CNTs, and SnPc-8OCH₃ @CNTs. Here, in addition to the unsubstituted

phthalocyanine tin (IV) Sn(OH)₂Pc, SnPc-8 F and SnPc-8OCH₃ were also chosen to fabricate composite catalysts owing to the typical electron-withdrawing and electron-donating substituent nature of -F and -OCH₃, which are able to effectively modulate the local electronic structure of the metal active sites and in turn optimize the catalytic property [65–67]. Inductively coupled plasma-mass spectrometry (ICP-MS) results disclose a Sn content of 0.50 ± 0.02 wt% for all three catalysts. No nanoparticles were observed in the scanning electron microscopy (SEM) and transmission electron microscopy (TEM) images of all three catalysts, suggesting the uniform dispersion of phthalocyanine molecules on the surface of CNTs in all three catalysts (Figs. S1 and S2). This is further supported by the wide distribution of Sn and N over the whole samples for all three catalysts according to the energy-dispersive X-ray spectroscopy (EDS) mapping images (Fig. 1b, Figs. S3 and S4). The dispersion of the phthalocyanine molecules on CNTs was further

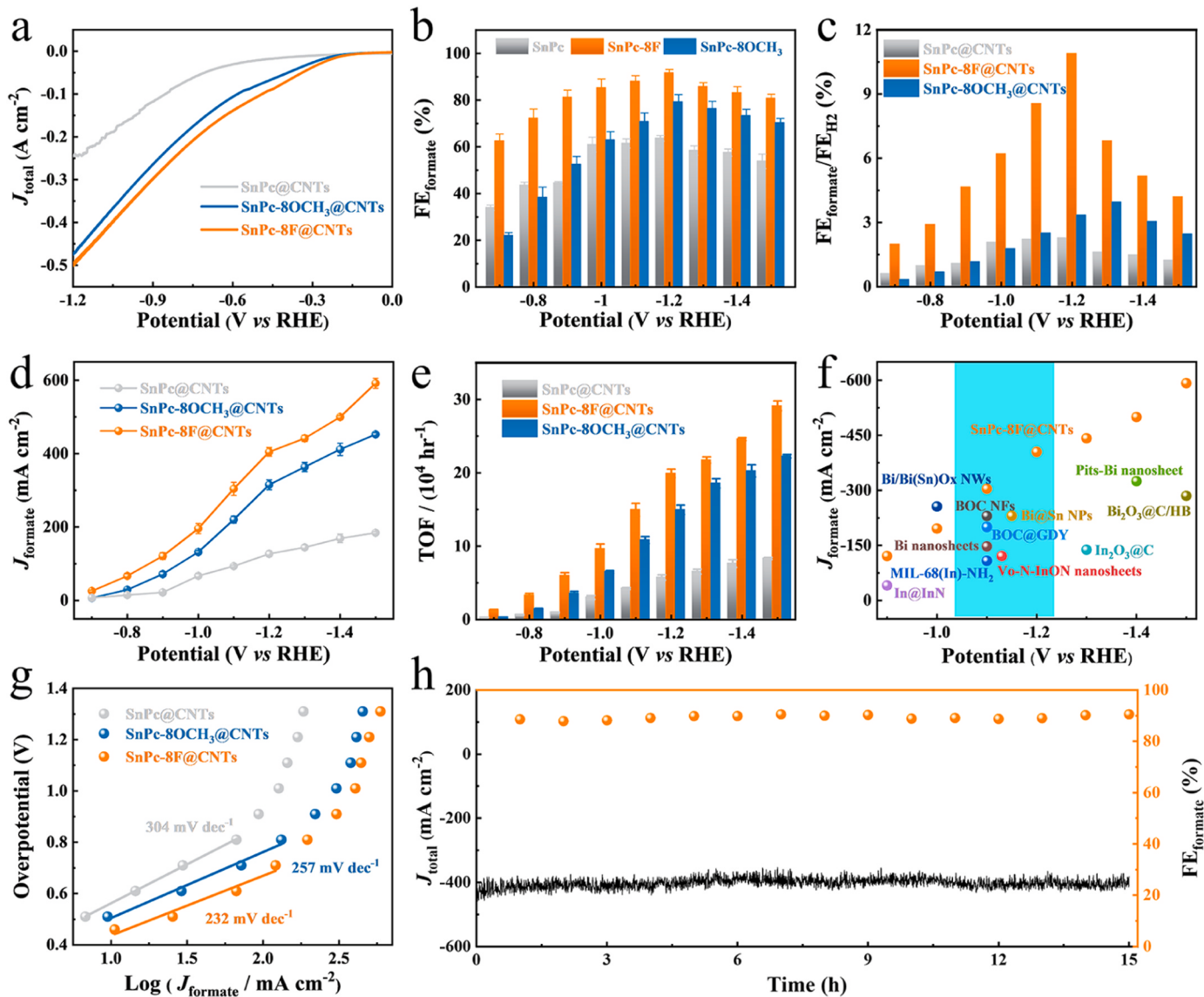


Fig. 2. (a) LSV curves of SnPc@CNTs, SnPc-8OCH₃ @CNTs, and SnPc-8 F@CNTs. (b) FE_{formate}, (c) FE_{formate}/FE_{H2} ratios, (d) J_{formate} , and (e) TOF of SnPc@CNTs, SnPc-8 F@CNTs, and SnPc-8OCH₃ @CNTs at various potentials. (f) Formate current density of SnPc-8 F@CNTs compared with those of other state-of-the-art CO₂ to formate reduction catalysts. (g) Tafel plots for SnPc@CNTs, SnPc-8OCH₃ @CNTs, and SnPc-8 F@CNTs. (h) Stability of SnPc-8 F@CNTs at a potential of -1.2 V versus RHE.

explored by the aberration-corrected high-angle annular dark-field scanning transmission electron microscopy (AC-HAAD-STEM) images. As displayed in Figs. 1c and S5, distinct brilliant spots can be noticed on the surface of CNTs for the three catalysts, illustrating the atomic dispersion of Sn sites. It is worth noting that several districts with dense bright spots were observed in the AC-HAAD-STEM image of SnPc@CNTs, suggesting the presence of Sn(OH)₂Pc molecule aggregation in this catalyst due to the poor solubility of unsubstituted Sn(OH)₂Pc molecules (Fig. S5a).

The valence state of Sn in the three composite catalysts was investigated by X-ray photoelectron spectroscopy (XPS). In the Sn 3d XPS spectra, SnPc@CNTs exhibit two peaks at 486.4 and 494.8 eV, corresponding to 3d_{5/2} and 3d_{3/2} of Sn⁴⁺, respectively (Fig. S6). [68,69] Owing to the electron-donating nature of the -OCH₃ substituent group, the peaks of Sn 3d_{5/2} and 3d_{3/2} for SnPc-8OCH₃ @CNTs shift to lower energy at 486.0 and 494.4 eV compared to SnPc@CNTs, implying a lower valence state of Sn in SnPc-8OCH₃ @CNTs (Fig. S6). SnPc-8 F@CNTs shows higher binding energy of 487.6 and 495.9 eV for Sn 3d than those for SnPc@CNTs due to the electron-withdrawing

nature of F substituent groups, suggesting a higher valence state of Sn in SnPc-8 F@CNTs (Fig. S6). The electronic structure and coordination environment of Sn in the three catalysts were further investigated by XANES tests. As can be seen in Fig. 1d, the pre-edge peaks of SnPc@CNTs, SnPc-8OCH₃ @CNTs, and SnPc-8 F@CNTs were observed at 29,201, 29,200.5, and 29,201.5 eV, respectively, in the Sn K-edge XANES spectra. This manifests that the order for the valence state of Sn in the three catalysts is SnPc-8 F@CNTs > SnPc@CNTs > SnPc-8OCH₃ @CNTs, agreeing well with the XPS results. Furthermore, the Fourier-transformed k²-weighted extended X-ray absorption fine structure (FT-EXAFS) and wavelet transform (WT) were employed to explore the local electronic structure of Sn. In the FT-EXAFS plots of Sn K-edge, all three materials exhibit the main peak at $\sim 1.56 \text{ \AA}$, corresponding to the Sn-N/O scattering path without observing the signal for the Sn-Sn bond at $\sim 2.79 \text{ \AA}$, indicating the atomic dispersion of Sn sites.

In all these three catalysts (Fig. 1e). In accordance, WT plots for the Sn K-edge EXAFS of all these three catalysts also display only characteristic intensity maximum from Sn-N/O scattering at $\sim 5 \text{ \AA}^{-1}$ (Figs. 1f and S7). In addition, EXAFS fitting has been performed to determine

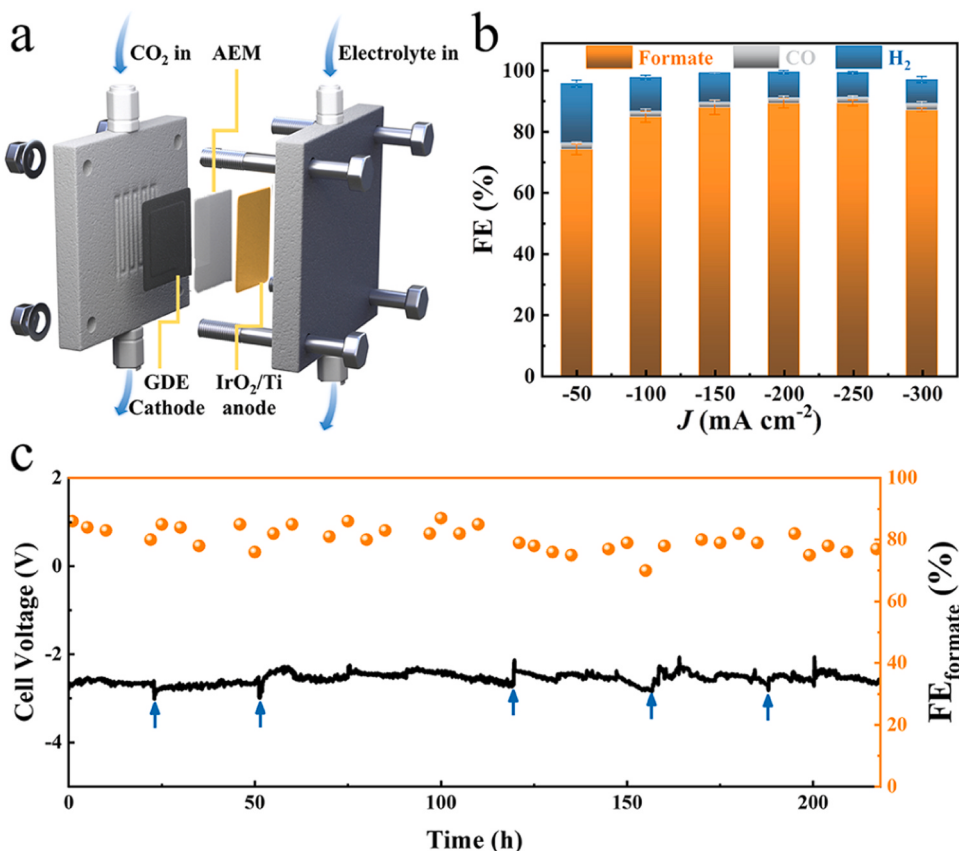


Fig. 3. (a) Schematic illustration of the MEA cell. (b) FEs of SnPc-8 F@CNTs at different current densities in the MEA cell with 1 M KHCO₃ as electrolyte. (c) Long-term stability of SnPc-8 F@CNTs in the MEA cell at -100 mA cm^{-2} with 1 M KHCO₃ as electrolyte. The vertical arrow marks the time of refreshing the electrolyte.

the coordination structure around the atomic Sn centers. As expected, the EXAFS fitting results for the first shell reveal that the Sn atom is coordinated by ~ 6 N/O atoms on average in all the three catalysts (Figs. S8–S10 and Table S1), in line with the Sn center, coordinated with four N and two O atoms found in SnPc(OH)₂ according to its single-crystal structure. [70] In addition, the matrix-assisted laser desorption/ionization time-of-flight mass spectra of Sn(OH)₂Pc, Sn(OH)₂[Pc(F)₈], and Sn(OH)₂[Pc(OCH₃)₈] show an intense signal of 665, 809, and 905, respectively, corresponding to their ions $[\text{M}]^+$ with Sn-N₄-O₂ sites, further indicating the Sn center coordinated with four N and two O atoms in SnPc@CNTs, SnPc-8 F@CNTs, and SnPc-8OCH₃ @CNTs (Figs. S11–S13).

3.2. Electrochemical measurements in flow cell

The CO₂RR performance of all the as-prepared catalysts was assessed by a three-compartment gas diffusion electrode (GDE)-based flow reactor cell (Fig. S14). Firstly, the electrochemical CO₂RR performance was evaluated by linear sweep voltammetry (LSV). As displayed in Fig. 2a, SnPc-8 F@CNTs exhibit a lower onset overpotential and larger current density than those for SnPc-8OCH₃ @CNTs and SnPc@CNTs, suggesting the highest catalytic activity of SnPc-8 F@CNTs among this series of catalysts. The CO₂RR activity and selectivity of all the catalysts were further obtained via constant potential electrolysis under a wide applied potential range from -0.7 to -1.5 V versus RHE (Figs. S15–S17). The gas and liquid products were analyzed using a gas chromatograph and ¹H nuclear magnetic resonance (¹H NMR), respectively (Figs. S18–S20). Fig. 2b displays the FE_{formate} of the electrolysis products against the applied potentials. As can be found, SnPc-8 F@CNTs exhibits a FE_{formate} of 62.5–91.7% at the applied potential range, while the FE_{formate} for SnPc-8OCH₃ @CNTs and SnPc@CNTs is 21.9–79.2% and

34.0–63.6%, respectively, under the same potential range, indicating the highest CO₂RR catalytic selectivity of SnPc-8 F@CNTs among these three catalysts. Moreover, the higher FE_{formate}/FE_{H2} and lower FE_{H2} and FE_{CO} for SnPc-8 F@CNTs than those for the other two catalysts under all the applied potentials further disclose the best catalytic selectivity of SnPc-8 F@CNTs towards formate generation (Figs. 2c, S21 and S22). In particular, a maximal FE_{formate} of 91.7% is achieved for SnPc-8 F@CNTs at -1.2 V versus RHE with a J_{formate} of 404 mA cm^{-2} , much higher than those for SnPc-8OCH₃ @CNTs (FE_{formate} = 79.2% and $J_{\text{formate}} = 315 \text{ mA cm}^{-2}$ at -1.2 V versus RHE) and SnPc@CNTs (FE_{formate} = 63.6% and $J_{\text{formate}} = 127 \text{ mA cm}^{-2}$ at -1.2 V versus RHE), clearly confirming the

superior catalytic activity of SnPc-8 F@CNTs towards CO₂-to-formate conversion (Fig. 2b and d). This is also supported by the fact that SnPc-8 F@CNTs shows larger J_{formate} at all the applied potentials compared to SnPc-8OCH₃ @CNTs and SnPc@CNTs (Fig. 2d), demonstrating the significant effect of the electron-withdrawing F atoms on improving the catalytic activity of SnPc-8 F@CNTs. Remarkably, SnPc-8 F@CNTs can deliver a J_{formate} of 600 mA cm^{-2} with a FE_{formate} of 80.8% under a higher applied potential of -1.5 V versus RHE, meeting the industrial current density requirements and indicating the great application potential of SnPc-8 F@CNTs in formate production from CO₂RR. It is worth noting that SnPc-8OCH₃ @CNTs display lower FE_{formate} than those of SnPc@CNTs at a potential range of 0.7 – 0.8 V versus RHE, suggesting the negative effect of the electron-donating -OCH₃ group on the catalytic activity of SnPc-8OCH₃ @CNTs towards CO₂-to-formate conversion (Fig. 2b). However, along with the applied potential negatively shifted, both FE_{formate} and J_{formate} of SnPc@CNTs become inferior to SnPc-8OCH₃ @CNTs due to the aggregation of SnPc molecules on the surface of CNTs in SnPc@CNTs derived from the poor solubility of SnPc. Additionally, two composite catalysts SnPc-8Cl@CNTs

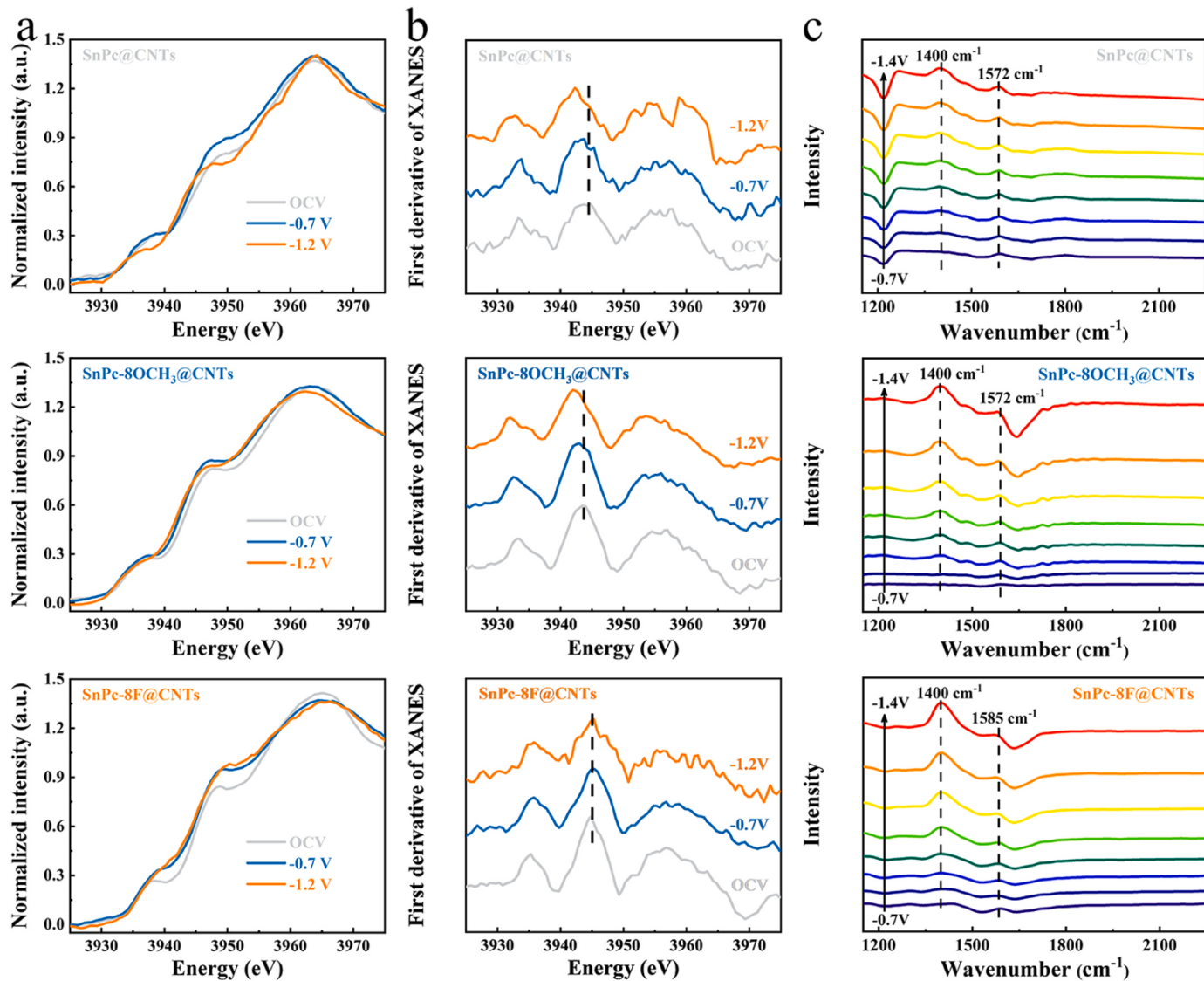


Fig. 4. (a) In situ Sn L₃-edge XANES spectra of SnPc@CNTs, SnPc-8OCH₃ @CNTs, and SnPc-8 F@CNTs at OCV and at -0.7 and -1.2 V versus RHE in CO₂-saturated 0.5 M NaHCO₃. (b) First derivatives of the spectra in (a). (c) In situ ATR-IR spectra of SnPc@CNTs, SnPc-8OCH₃ @CNTs, and SnPc-8 F@CNTs at different potentials in CO₂-saturated 0.5 M KHCO₃.

and SnPc-8OC₅H₁₁ @CNTs were fabricated from 2,3,9,10,16,17,23,24-octachlorophthalocyanine tin (IV) {Sn(OH)₂[Pc(Cl)₈]} and 2,3,9,10,16,17,23,24-octapentyloxyphthalocyanine tin (IV) {Sn(OH)₂[Pc(OC₅H₁₁)₈]}, respectively, to clarify the geometric effect of substituents on the CO₂RR performance (Fig. S23). Electrochemical tests indicate SnPc-8Cl@CNTs with similar substituent size to that of SnPc-8 F@CNTs exhibits inferior CO₂RR performance compared to SnPc-8 F@CNTs due to the weaker electron-withdrawing effect of Cl atoms compared to F atoms (Fig. S24). Moreover, although the substituent size in SnPc-8OC₅H₁₁ @CNTs is much larger than that for SnPc-8OCH₃ @CNTs, the CO₂RR performance of SnPc-8OC₅ @CNTs is close to that revealed for SnPc-8OCH₃ @CNTs (Fig. S25). These findings manifest the insignificant influence of geometric effect of the substituting groups on the CO₂RR properties of the prepared catalysts.

The superior catalytic activity of SnPc-8 F@CNTs is also gleaned from its larger turnover frequency (TOF) of 291278 h⁻¹ for formate at -1.5 V versus RHE compared with SnPc-8OCH₃ @CNTs (222,644 h⁻¹ at -1.5 V versus RHE) and SnPc@CNTs (83,340 h⁻¹ at -1.5 V versus RHE) (Fig. 2e). In addition, SnPc-8 F@CNTs shows a smaller Tafel slope of 232 mV/decade compared to SnPc-8OCH₃ @CNTs (257 mV/decade) and SnPc@CNTs (304 mV/decade), indicating the faster kinetics of

SnPc-8 F@CNTs (Fig. 2g). More importantly, SnPc-8 F@CNTs exhibits considerable stability as revealed by the current density retention of 90% and almost unchanged FE_{formate} after 15 h of continuous electrolysis operation at -1.2 V versus RHE (Fig. 2h). Moreover, the morphology and component of SnPc-8 F@CNTs after long-term CO₂RR test are retained, further confirming the stability of SnPc-8 F@CNTs (Figs. S26-S28). This, in combination with its high FE_{formate} and large J_{formate}, enables SnPc-8 F@CNTs to be comparable to the thus far state-of-the-art catalysts for formate production from CO₂RR (Fig. 2f).

3.3. Electrochemical measurements in MEA cell

The full cell performance of all three composite catalysts was evaluated by using a zero-gap MEA cell with the three composite materials as the cathode catalyst and IrO₂/Ti mesh as the anode catalyst (Figs. 3a and S29). Fig. S30 shows the LSV curves recorded in the MEA cell. As can be found, with 1 M KHCO₃ as the electrolyte, SnPc-8 F@CNTs displays the highest current densities at the voltage range of 2.0–3.0 V among all the three catalysts, implying its superior CO₂RR performance to SnPc@CNTs and SnPc-8OCH₃ @CNTs. Constant current electrolysis at various

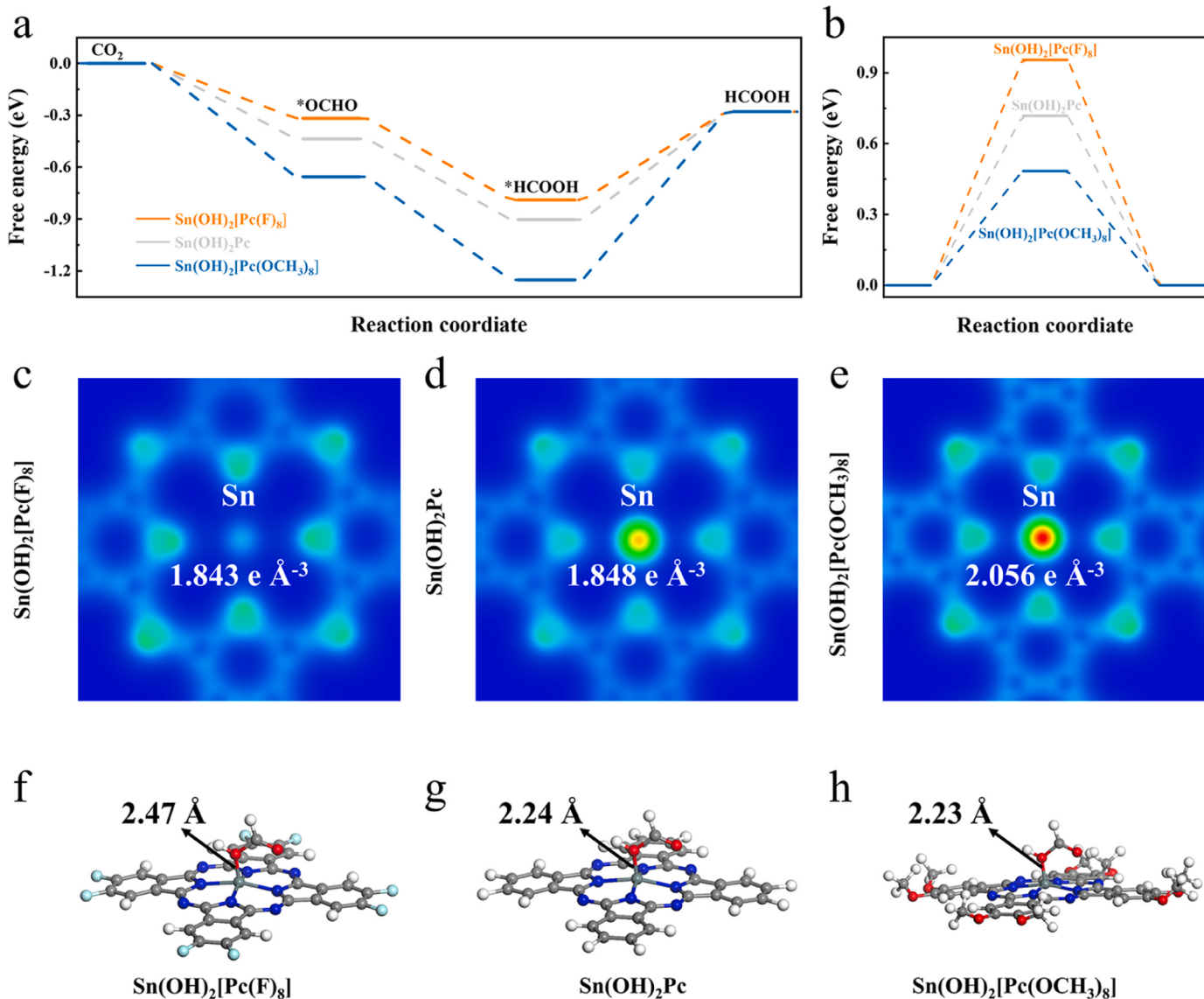


Fig. 5. Free energy diagrams in CO₂RR for production of (a) HCOOH and (b) H₂ on Sn(OH)₂[Pc(F)₈], Sn(OH)₂Pc, and Sn(OH)₂[Pc(OCH₃)₈]. (c) Charge density differences (the cyan and orange indicate electron accumulation and depletion) of (c) Sn(OH)₂[Pc(F)₈], (d) Sn(OH)₂Pc, and (e) Sn(OH)₂[Pc(OCH₃)₈]. Optimized geometries of *HCOOH on (f) Sn(OH)₂[Pc(F)₈], (g) Sn(OH)₂Pc, and (h) Sn(OH)₂[Pc(OCH₃)₈].

current densities of 50–300 mA cm⁻² was further carried out to explore the full cell performance of these catalysts in MEA cell (Fig. 3b and Fig. S31). Formate is still the primary product for SnPc-8 F@CNTs at all the applied current densities with a maximal FE_{formate} of 90% at ~200 mA cm⁻², significantly higher than that for SnPc-8OCH₃@CNTs (maximal FE_{formate} = 73% at ~150 mA cm⁻²) and SnPc@CNTs (maximal FE_{formate} = 59% at ~150 mA cm⁻²), further confirming the superior catalytic activity of SnPc-8 F@CNTs. More importantly, SnPc-8 F@CNTs can deliver a current density of ~100 mA cm⁻² under a full-cell voltage of ca. 2.6 V with a FE_{formate} of 85% for 200 h stable electrolysis (Fig. 3c), indicating the great practical application potential of SnPc-8 F@CNTs towards electrocatalysis CO₂RR.

4. Mechanistic insights of SnPc@CNTs

To deeply understand the effect of the substituent groups on the performance of the as-prepared catalysts, in situ XAS measurements were conducted (Fig. S32). As shown in Fig. 4a, SnPc-8 F@CNTs, SnPc@CNTs, and SnPc-8OCH₃@CNTs show rising edge energy of ~3944.8, 3944.3, and 3943.5 eV, respectively, at an open-circuit

voltage (OCV) in their Sn L₃-edge XANES spectra, indicating the highest oxidation state of Sn in SnPc-8 F@CNTs among this series of catalysts, agreeing well with the Sn K-edge EXAFS analysis results as detailed above [71,72]. In particular, the rising edge energy of SnPc-8 F@CNTs kept almost unchanged when holding SnPc-8 F@CNTs electrode at ~0.7 V and ~1.2 V versus RHE, revealing its excellent resistance to structural change during the reduction process and favoring high electrochemical activity and stability (Fig. 4a and b). In contrast, both SnPc@CNTs and SnPc-8OCH₃@CNTs show an obvious negative shift in the rising edge energy at ~0.7 V and ~1.2 V versus RHE compared to those at OCV (Fig. 4a and b). Nevertheless, holding the SnPc@CNTs and SnPc-8OCH₃@CNTs electrodes at the OCV after the reaction only partially restored the spectral shape in comparison with the corresponding fresh electrodes (Fig. S33), indicating the irreversible structural changes of the Sn centers in SnPc@CNTs and SnPc-8OCH₃@CNTs during the reduction process. These results are consistent with the better electrochemical performance revealed for SnPc-8 F@CNTs than SnPc@CNTs and SnPc-8OCH₃@CNTs.

To further unravel the catalytic intermediates, in situ ATR-IR was employed to monitor the CO₂RR process on the different catalysts

(Fig. S34). As shown in Figs. 4c and S35, on scanning the applied potential from -0.7 to -1.4 V versus RHE, all the three catalysts exhibit an upward peak at ca. 1400 and 1572 cm^{-1} ascribed to $^*\text{OCHO}$ and $^*\text{HCOOH}$ species without the signal due to $^*\text{CO}$ species at 2050 cm^{-1} in their *in situ* ATR-IR spectra, revealing the dominant CO_2 reduction product of formate for these catalysts, in line with the experimental finding. [73,74] Moreover, the band intensities of $^*\text{OCHO}$ and $^*\text{HCOOH}$ species increased along with the gradual increase in the applied potentials, consistent with the trend of formate formation rates. These results.

suggest the CO_2 reduction pathway of $\text{CO}_2^* \rightarrow ^*\text{OCHO} \rightarrow ^*\text{HCOOH}$ for all three catalysts. It is noteworthy that the signals of the $^*\text{OCHO}$ and $^*\text{HCOOH}$ species start to appear at a more positive potential of -0.7 V versus RHE for SnPc-8 F@CNTs compared to SnPc@CNTs (-0.7 V versus RHE) and SnPc-8OCH₃@CNTs (-0.9 V versus RHE), suggesting a lower onset overpotential of SnPc-8 F@CNTs for CO_2RR .

To further gain insights into the reaction mechanism for the CO_2RR on the as-prepared three SnPc-based catalysts, the free energies of the CO_2RR pathway were calculated on $\text{Sn}(\text{OH})_2\text{Pc}$, $\text{Sn}(\text{OH})_2[\text{Pc}(\text{F})_8]$, and $\text{Sn}(\text{OH})_2[\text{Pc}(\text{OCH}_3)_8]$ by density functional theory (DFT). As shown in Fig. 5a, the desorption process of $^*\text{HCOOH}$ was disclosed to act as the potential limiting step for CO_2 -to-HCOOH conversion on all the three model catalysts. In particular, $\text{Sn}(\text{OH})_2[\text{Pc}(\text{F})_8]$ displays a lower energy barrier of 0.51 eV for $^*\text{HCOOH}$ desorption than those for $\text{Sn}(\text{OH})_2\text{Pc}$ (0.62 eV) and $\text{Sn}(\text{OH})_2[\text{Pc}(\text{OCH}_3)_8]$ (0.97 eV), revealing the faster CO_2RR kinetics of $\text{Sn}(\text{OH})_2[\text{Pc}(\text{F})_8]$ compared to $\text{Sn}(\text{OH})_2\text{Pc}$ and $\text{Sn}(\text{OH})_2[\text{Pc}(\text{OCH}_3)_8]$. Moreover, the free energies of HER on $\text{Sn}(\text{OH})_2[\text{Pc}(\text{F})_8]$, $\text{Sn}(\text{OH})_2\text{Pc}$, and $\text{Sn}(\text{OH})_2[\text{Pc}(\text{OCH}_3)_8]$ were also calculated (Fig. 5b). It can be found that all the three model catalysts exhibit a lower energy barrier for CO_2RR than that for HER, manifesting the high selectivity for CO_2RR on these three model catalysts. In particular, the energy barrier of HER on $\text{Sn}(\text{OH})_2[\text{Pc}(\text{F})_8]$ ($\Delta G = 0.95$ eV) is higher than those for $\text{Sn}(\text{OH})_2\text{Pc}$ ($\Delta G = 0.72$ eV) and $\text{Sn}(\text{OH})_2[\text{Pc}(\text{OCH}_3)_8]$ ($\Delta G = 0.48$ eV), revealing the inferior HER activity of $\text{Sn}(\text{OH})_2[\text{Pc}(\text{F})_8]$, in favor of CO_2RR . In addition, according to the calculation results, the lowest unoccupied molecular orbitals (LUMO) and the highest occupied molecular orbital (HOMO) of $\text{Sn}(\text{OH})_2[\text{Pc}(\text{F})_8]$ negatively shift to -9.49 eV and -12.54 eV compared to unsubstituted $\text{Sn}(\text{OH})_2\text{Pc}$ (-8.59 eV and -11.94 eV) owing to its eight peripherally substituted electron-withdrawing F atoms, leading to a lower electron density of $+1.843\text{ e } \text{\AA}^{-3}$ around the Sn active site for $\text{Sn}(\text{OH})_2[\text{Pc}(\text{F})_8]$ than that for $\text{Sn}(\text{OH})_2\text{Pc}$, $+1.848\text{ e } \text{\AA}^{-3}$ (Figs. 5c and d, S36). In contrast, $\text{Sn}(\text{OH})_2[\text{Pc}(\text{OCH}_3)_8]$ exhibits larger LUMO and HOMO (-8.31 eV and -11.24 eV) than those of unsubstituted SnPc owing to the electron-donating nature of the -OCH₃ groups, affording the electron-rich environment of Sn in $\text{Sn}(\text{OH})_2[\text{Pc}(\text{OCH}_3)_8]$ with a higher electron density of $+2.056\text{ e } \text{\AA}^{-3}$ (Figs. 5e and S36). Nevertheless, the lowest electron density around the Sn atom in $\text{Sn}(\text{OH})_2[\text{Pc}(\text{F})_8]$ suggests the weakest bonding of $^*\text{HCOOH}$ during the electrocatalytic CO_2RR process, which is further supported by the longer distance of 2.47 \AA between the $^*\text{HCOOH}$ oxygen atom and Sn atom for $\text{Sn}(\text{OH})_2[\text{Pc}(\text{F})_8]$ than those for $\text{Sn}(\text{OH})_2\text{Pc}$ (2.24 \AA) and $\text{Sn}(\text{OH})_2[\text{Pc}(\text{OCH}_3)_8]$ (2.23 \AA) (Fig. 5f-h). These results are agreeing well with the calculated lower energy barrier for $^*\text{HCOOH}$ desorption on $\text{Sn}(\text{OH})_2[\text{Pc}(\text{F})_8]$ than those on $\text{Sn}(\text{OH})_2\text{Pc}$ and $\text{Sn}(\text{OH})_2[\text{Pc}(\text{OCH}_3)_8]$, demonstrating the significant effect of the electron-withdrawing F atoms on improving the CO_2RR catalytic activity of $\text{Sn}(\text{OH})_2[\text{Pc}(\text{F})_8]$.

5. Conclusion

In summary, supporting SnPcs on multi-walled CNTs through π - π stacking affords a series of composite catalysts with remarkable electrocatalytic properties for CO_2 -to-formate conversion. In particular, with the fine-tuning of pendant groups on the phthalocyanine ligand, SnPc-8 F@CNTs exhibits comparable performance to the thus far state-of-the-art catalysts for formate production from CO_2RR in terms of both activity and selectivity, demonstrating the significant effect of the

electron-withdrawing F groups on improving the catalytic activity. This work should be helpful in developing high-efficiency electrocatalysts for converting CO_2 into value-added chemicals with promising applications.

CRediT authorship contribution statement

Baotong Chen: Software, Formal analysis, Investigation, Visualization, Writing – original draft. **Haiyuan Zou, Lei Gong:** Performed Software, Formal analysis. **Hao Zhang, Ning Li, Houhe Pan:** Performed Visualization. **Kang Wang:** Performed Methodology, Validation, Writing – review & editing, Supervision. **Tao Yang, Yunpeng Liu, Lele Duan** performed Resources. **Jianzhuang Jiang:** Performed Project administration, Funding acquisition.

Declaration of Competing Interest

The authors declare that they have no known competing financial interests or personal relationships that could have appeared to influence the work reported in this paper.

Data availability

Data will be made available on request.

Acknowledgments

This work was financially supported by the Natural Science Foundation of China (Nos. 22235001 and 22175020) and Interdisciplinary Research Project for Young Teachers of USTB (No. FRF-IDRY-21-028).

Appendix A. Supporting information

Supplementary data associated with this article can be found in the online version at doi:10.1016/j.apcatb.2023.123650.

References

- [1] Y.Y. Birdja, E. Perez-Gallent, M.C. Figueiredo, A.J. Gottle, F. Calle-Vallejo, M.T. M. Koper, Advances and challenges in understanding the electrocatalytic conversion of carbon dioxide to fuels, Nat. Energy 4 (2019) 732–745, <https://doi.org/10.1038/s41560-019-0450-y>.
- [2] X. Zhi, A. Vasileff, Y. Zheng, Y. Jiao, S.Z. Qiao, Role of oxygen-bound reaction intermediates in selective electrochemical CO_2 reduction, Energy Environ. Sci. 14 (2021) 3912–3930, <https://doi.org/10.1039/D1EE00740H>.
- [3] S. Lin, C.S. Diercks, Y.B. Zhang, N. Kornienko, E.M. Nichols, Y.B. Zhao, A.R. Paris, D. Kim, P. Yang, O.M. Yaghi, C.J. Chang, Covalent organic frameworks comprising cobalt porphyrins for catalytic CO_2 reduction in water, Science 349 (2015) 1208–1213, <https://doi.org/10.1126/science.aac8343>.
- [4] D.F. Gao, R.M. Aran-Ais, H.S. Jeon, B. Roldan Cuanya, Rational catalyst and electrolyte design for CO_2 electroreduction towards multicarbon products, Nat. Catal. 2 (2019) 198–210, <https://doi.org/10.1038/s41929-019-0235-5>.
- [5] D.F. Gao, H. Zhou, J. Wang, S. Miao, F. Yang, G. Wang, J. Wang, X.H. Bao, Size-dependent electrocatalytic reduction of CO_2 over Pd nanoparticles, J. Am. Chem. Soc. 137 (2015) 4288–4291, <https://doi.org/10.1021/jacs.5b00046>.
- [6] S. Nitopi, E. Bertheussen, S.B. Scott, X. Liu, A.K. Engstfeld, S. Horch, B. Seger, I.E. L. Stephens, K. Chan, C. Hahn, J.K. Norskov, T.F. Jaramillo, I. Chorkendorff, Progress and perspectives of electrochemical CO_2 reduction on copper in aqueous electrolyte, Chem. Rev. 119 (2019) 7610–7672, <https://doi.org/10.1021/cracs.8b00705>.
- [7] X.B. Zheng, P. Li, S.X. Dou, W.P. Sun, H.G. Pan, D.S. Wang, Y.D. Li, Non-carbon-supported single-atom site catalysts for electrocatalysis, Energy Environ. Sci. 14 (2021) 2809–2858, <https://doi.org/10.1039/D1EE00248A>.
- [8] S.B. Liu, J. Xiao, X.F. Lu, J. Wang, X. Wang, X.W. Lou, Efficient electrochemical reduction of CO_2 to HCOOH over sub-2nm SnO_2 quantum wires with exposed grain boundaries, Angew. Chem. Int. Ed. 58 (2019) 8499–8503, <https://doi.org/10.1002/anie.201903613>.
- [9] C. Xia, P. Zhu, Q. Jiang, Y. Pan, W.T. Liang, E. Stavitsk, H.N. Alshareef, H.T. Wang, Continuous production of pure liquid fuel solutions via electrocatalytic CO_2 reduction using solid-electrolyte devices, Nat. Energy 4 (2019) 776–785, <https://doi.org/10.1038/s41560-019-0451-x>.
- [10] Q.G. Zhu, J. Ma, X.C. Kang, X.F. Sun, H.Z. Liu, J.Y. Hu, Z.M. Liu, B.X. Han, Efficient reduction of CO_2 into formic acid on a lead or tin electrode using an ionic liquid catholyte mixture, Angew. Chem. Int. Ed. 55 (2016) 9012–9016, <https://doi.org/10.1002/anie.201601974>.

- [11] L. Lin, X.Y. He, X.G. Zhang, W.C. Ma, B. Zhang, D.Y. Wei, S.J. Xie, Q.H. Zhang, X. D. Yi, Y. Wang, A nanocomposite of bismuth clusters and $\text{Bi}_2\text{O}_3\text{CO}_3$ sheets for highly efficient electrocatalytic reduction of CO_2 to formate, e202214959, *Angew. Chem. Int. Ed.* 135 (2022), <https://doi.org/10.1002/ange.202214959>.
- [12] H.F. Liu, J. Xia, N. Zhang, H. Cheng, W. Bi, X.L. Zu, W.S. Chu, H.A. Wu, C.Z. Wu, Y. Xie, Solid-liquid phase transition induced electrocatalytic switching from hydrogen evolution to highly selective CO_2 reduction, *Nat. Catal.* 4 (2021) 202–211, <https://doi.org/10.1038/s41929-021-00576-3>.
- [13] T.T. Zheng, C.X. Liu, C.X. Guo, M.L. Zhang, X. Li, Q. Jiang, W.Q. Xue, H.L. Li, A. W. Li, C.W. Pao, J.P. Xiao, C.A. Xia, J. Zeng, Copper-catalysed exclusive CO_2 to pure formic acid conversion via single-alloy alloying, *Nat. Nanotechnol.* 16 (2021) 1386–1393, <https://doi.org/10.1038/s41565-021-00974-5>.
- [14] J.Y. Li, J.X. Li, X.L. Liu, J.C. Chen, P.F. Tian, S. Dai, M.H. Zhu, Y.F. Han, Probing the role of surface hydroxyls for Bi, Sn and In catalysts during CO_2 Reduction, *Appl. Catal. B Environ.* 298 (2021), 120581, <https://doi.org/10.1016/j.apcatb.2021.120581>.
- [15] X.L. Zheng, P. De Luna, F.P.G. de Arquer, B. Zhang, N. Becknell, M.B. Ross, Y.F. Li, M.N. Banis, Y.Z. Li, M. Liu, O. Voznyy, C.T. Dinh, T.T. Zhuang, P. Stadler, Y. Cui, X. W. Du, P.D. Yang, E.H. Sargent, Sulfur-modulated tin sites enable highly selective electrochemical reduction of CO_2 to formate, *Joule* 1 (2017) 794–805, <https://doi.org/10.1016/j.joule.2017.09.014>.
- [16] S. Yan, C. Peng, C. Yang, Y. Chen, J. Zhang, A.X. Guan, X.M. Lv, H. Wang, Z. Wang, T.K. Sham, Q. Han, G.F. Zheng, Electron localization and lattice strain induced by surface lithium doping enable ampere-level electrosynthesis of formate from CO_2 , *Angew. Chem. Int. Ed.* 60 (2021) 25741–25745, <https://doi.org/10.1002/anie.202111351>.
- [17] P.F. Yin, J. Fu, Q. Yun, B. Chen, G. Liu, L. Li, Z. Huang, Y. Ge, H. Zhang, Preparation of amorphous SnO_2 -encapsulated multiphased crystalline Cu heterostructures for highly efficient CO_2 reduction, *Adv. Mater.* 34 (2022), 2201114, <https://doi.org/10.1002/adma.202201114>.
- [18] W.C. Ma, S.J. Xie, X.G. Zhang, F.F. Sun, J. Kang, Z. Jiang, Q. Zhang, D.Y. Wu, Y. Wang, Promoting electrocatalytic CO_2 reduction to formate via sulfur-boosting water activation on indium surfaces, *Nat. Commun.* 10 (2019) 892, <https://doi.org/10.1038/s41467-019-108805-x>.
- [19] Y. Huang, X.N. Mao, G.T. Yuan, D. Zhang, B.B. Pan, J. Deng, Y.R. Shi, N. Han, C. R. Li, L. Zhang, L. Wang, L. He, Y.Y. Li, Y.G. Li, Size-dependent selectivity of electrochemical CO_2 reduction on converted In_2O_3 nanocrystals, *Angew. Chem. Int. Ed.* 60 (2021) 15844–15848, <https://doi.org/10.1002/anie.202105256>.
- [20] J.B. Zhang, R.G. Yin, Q. Shao, T. Zhu, X.Q. Huang, Oxygen vacancies in amorphous InO_x nanoribbons enhance CO_2 adsorption and activation for CO_2 electroreduction, *Angew. Chem. Int. Ed.* 58 (2019) 5609–5613, <https://doi.org/10.1002/anie.201900167>.
- [21] D. Yao, C. Tang, A. Vasileff, X. Zhi, Y. Jiao, S.Z. Qiao, The controllable reconstruction of Bi-MOFs for electrochemical CO_2 reduction through electrolyte and potential mediation, *Angew. Chem. Int. Ed.* 60 (2021) 18178–18184, <https://doi.org/10.1002/anie.202104747>.
- [22] Y. Liu, Z.X. Lou, X. Wu, B. Mei, J. Chen, J.Y. Zhao, J. Li, H.Y. Yuan, M. Zhu, S. Dai, C. Sun, P.F. Liu, Z. Jiang, H.G. Yang, Molecularly distorted local structure in Bi_2CuO_4 oxide to stabilize lattice oxygen for efficient formate electrosynthesis, *Adv. Mater.* 34 (2022), 2202568, <https://doi.org/10.1002/adma.202202568>.
- [23] Y.T. Wang, Y.H. Li, J.Z. Liu, C.X. Dong, C.Q. Xiao, L. Cheng, H.L. Jiang, H. Jiang, C. Z. Li, BiPO₄-derived 2D nanosheets for efficient electrocatalytic reduction of CO_2 to liquid fuel, *Angew. Chem. Int. Ed.* 60 (2021) 7681–7685, <https://doi.org/10.1002/anie.202014341>.
- [24] X. Zhang, T. Lei, Y.Y. Liu, J.L. Qiao, Enhancing CO_2 electrolysis to formate on facilely synthesized Bi catalysts at low overpotential, *Appl. Catal. B Environ.* 218 (2017) 46–50, <https://doi.org/10.1016/j.apcatb.2017.06.032>.
- [25] Z.L. Jiang, T. Wang, J.J. Pei, H.S. Shang, D.N. Zhou, H.J. Li, J.C. Dong, Y. Wang, R. Cao, Z.B. Zhuang, W.X. Chen, D.S. Wang, J.T. Zhang, Y.D. Li, Discovery of main group single Sb-N₄ active sites for CO_2 electroreduction to formate with high efficiency, *Energy Environ. Sci.* 13 (2020) 2856–2863, <https://doi.org/10.1039/d0ee01486a>.
- [26] Y.M. Shi, Y. Ji, J. Long, Y. Liang, Y. Liu, Y.F. Yu, J.P. Xiao, B. Zhang, Unveiling hydrocerussite as an electrochemically stable active phase for efficient carbon dioxide electroreduction to formate, *Nat. Commun.* 11 (2020) 3415, <https://doi.org/10.1038/s41467-020-17120-9>.
- [27] L. Jia, M.Z. Sun, J. Xu, X. Zhao, R. Zhou, B.B. Pan, L. Wang, N. Han, B.L. Huang, Y. G. Li, Phase-dependent electrocatalytic CO_2 reduction on Pd_3Bi nanocrystals, *Angew. Chem. Int. Ed.* 60 (2021) 21741–21745, <https://doi.org/10.1002/anie.202109288>.
- [28] T.W. Jiang, X.X. Qin, K. Ye, W.Y. Zhang, H. Li, W.H. Liu, S.J. Huo, X.G. Zhang, K. Jiang, W.B. Cai, An interactive study of catalyst and mechanism for electrochemical CO_2 reduction to formate on Pd surfaces, *Appl. Catal. B Environ.* 334 (2023), 122815, <https://doi.org/10.1016/j.apcatb.2023.122815>.
- [29] J. Li, Y. Kuang, Y.T. Meng, X. Tian, W.H. Hung, X. Zhang, A. Li, M. Xu, W. Zhou, C. S. Ku, C.Y. Chiang, G.L. Zhu, J. Guo, X.F. Sun, H.J. Dai, Electrocatalysis of CO_2 to formate on a copper-based electrocatalyst at high pressures with high energy conversion efficiency, *J. Am. Chem. Soc.* 142 (2020) 7276–7282, <https://doi.org/10.1021/jacs.0c00122>.
- [30] L. Lv, X.B. He, J.S. Wang, Y.J. Ruan, S.X. Ouyang, H. Yuan, T.R. Zhang, Charge localization to optimize reactant adsorption on $\text{KCu}_4\text{S}_4/\text{CuO}$ interfacial structure toward selective CO_2 electroreduction, *Appl. Catal. B Environ.* 298 (2021), 120531, <https://doi.org/10.1016/j.apcatb.2021.120531>.
- [31] D.R. Yang, S.W. Zuo, H.Z. Yang, X. Wang, Single-unit-cell catalysis of CO_2 electroreduction over Sub-1 nm Cu_9S_5 nanowires, *Adv. Energy Mater.* 11 (2021), 2100272, <https://doi.org/10.1002/aenm.202100272>.
- [32] W.B. Wang, Z.T. Wang, R.O. Yang, J.Y. Duan, Y.W. Liu, A.M. Nie, H.Q. Li, B.Y. Xia, T.Y. Zhai, In situ phase separation into coupled interfaces for promoting CO_2 electroreduction to formate over a wide potential window, *Angew. Chem. Int. Ed.* 60 (2021) 22940–22947, <https://doi.org/10.1002/anie.202110000>.
- [33] D.N. Wang, T.T. Sun, L.B. Xu, L. Gong, B.T. Chen, P.P. Zhang, T.Y. Zheng, Q.M. Xu, H.H. Pan, Y.X. Zhang, J.Z. Jiang, Interfacial engineering of $\text{SnO}_2/\text{Bi}_2\text{O}_3\text{CO}_3$ heterojunction on heteroatoms-doped carbon for high-performance CO_2 electroreduction to formate, *Nano Res.* 16 (2022) 2278–2285, <https://doi.org/10.1007/s12274-022-5058-z>.
- [34] Q. Yang, Q.L. Wu, Y. Liu, S.P. Luo, X.T. Wu, X.X. Zhao, H.Y. Zou, B.H. Long, W. Chen, Y.J. Liao, L.X. Li, P.K. Shen, L.L. Duan, Z.W. Quan, Novel Bi-doped amorphous SnO_x nanoshells for efficient electrochemical CO_2 reduction into formate at low overpotentials, *Adv. Mater.* 32 (2020), 2002822, <https://doi.org/10.1002/adma.202002822>.
- [35] T. Chen, T. Liu, T. Ding, B.B. Pang, L. Wang, X.K. Liu, X.Y. Shen, S.C. Wang, D. Wu, D. Liu, L.L. Cao, Q.Q. Luo, W. Zhang, W.K. Zhu, T. Yao, Surface oxygen injection in tin disulfide nanosheets for efficient CO_2 electroreduction to formate and syngas, *Nano-Micro Lett.* 13 (2021) 189, <https://doi.org/10.1007/s40820-021-00703-6>.
- [36] Z.P. Chen, X.X. Zhang, M.Y. Jiao, K.W. Mou, X.P. Zhang, L.C. Liu, Engineering electronic structure of stannous sulfide by amino-functionalized carbon: toward efficient electrocatalytic reduction of CO_2 to formate, *Adv. Energy Mater.* 10 (2020), 1903664, <https://doi.org/10.1002/aenm.201903664>.
- [37] W. Luc, C. Collins, S.W. Wang, H.L. Xin, K. He, Y.J. Kang, F. Jiao, Ag-Sn bimetallic catalyst with a core-shell structure for CO_2 reduction, *J. Am. Chem. Soc.* 139 (2017) 1885–1893, <https://doi.org/10.1021/jacs.6b10435>.
- [38] L.C.P. Perez, D. Teschner, E. Willinger, A. Guiet, M. Driess, P. Strasser, A. Fischer, In situ formed " $\text{Sn}_{1-x}\text{In}_x@\text{In}_{1-y}\text{Sn}_y\text{O}_z$ " core@shell nanoparticles as electrocatalysts for CO_2 reduction to formate, *Adv. Funct. Mater.* 31 (2021), 2103601, <https://doi.org/10.1002/adfm.202103601>.
- [39] D.M. Weekes, D.A. Salvatore, A. Reyes, A.X. Huang, C.P. Berlinguet, Electrolytic CO_2 Reduction in a Flow Cell, *Acc. Chem. Res.* 51 (2018) 910–918, <https://doi.org/10.1021/acs.accounts.8b00010>.
- [40] T. Burdyny, W.A. Smith, CO_2 reduction on gas-diffusion electrodes and why catalytic performance must be assessed at commercially-relevant conditions, *Energy Environ. Sci.* 12 (2019) 1442–1453, <https://doi.org/10.1039/c8ee03134g>.
- [41] Z.P. Zhang, J.T. Sun, F. Wang, L.M. Dai, Efficient oxygen reduction reaction (ORR) catalysts based on single iron atoms dispersed on a hierarchically structured porous carbon framework, *Angew. Chem. Int. Ed.* 57 (2018) 9038–9043, <https://doi.org/10.1002/anie.201804958>.
- [42] J.Y. Chen, H. Li, C. Fan, Q.W. Meng, Y.W. Tang, X.Y. Qiu, G.T. Fu, T.Y. Ma, Dual single-atomic Ni-N₄ and Fe-N₄ sites constructing janus hollow graphene for selective oxygen electrocatalysis, *Adv. Mater.* 32 (2020), 2003134, <https://doi.org/10.1002/adma.202003134>.
- [43] M.L. Xiao, J.B. Zhu, G.R. Li, N. Li, S. Li, Z.P. Cano, L. Ma, P.X. Cui, P. Xu, G. P. Jiang, H.L. Jin, S. Wang, T.P. Wu, J. Lu, A.P. Yu, D. Su, Z.W. Chen, A single-atom iridium heterogeneous catalyst in oxygen reduction reaction, *Angew. Chem. Int. Ed.* 58 (2019) 9640–9645, <https://doi.org/10.1002/anie.201905241>.
- [44] X.P. Yin, H.J. Wang, S.F. Tang, X.L. Lu, M. Shu, R. Si, T.B. Lu, Engineering the coordination environment of single-atom platinum anchored on graphdiyne for optimizing electrocatalytic hydrogen evolution, *Angew. Chem. Int. Ed.* 57 (2018) 9382–9386, <https://doi.org/10.1002/anie.201804817>.
- [45] S.H. Ye, F.Y. Luo, Q.L. Zhang, P.Y. Zhang, T.T. Xu, Q. Wang, D.S. He, L.C. Guo, Y. Zhang, C.X. He, X.P. Ouyang, M. Gu, J.H. Liu, X.L. Sun, Highly stable single Pt atomic sites anchored on aniline-stacked graphene for hydrogen evolution reaction, *Energy Environ. Sci.* 12 (2019) 1000–1007, <https://doi.org/10.1039/c8ee02888e>.
- [46] Y.W. Chen, R. Ding, J. Li, J.G. Liu, Highly active atomically dispersed platinum-based electrocatalyst for hydrogen evolution reaction achieved by defect anchoring strategy, *Appl. Catal. B Environ.* 301 (2022), 120830, <https://doi.org/10.1016/j.apcatb.2021.120830>.
- [47] H.B. Yang, S.F. Hung, S. Liu, K.D. Yuan, S. Miao, L.P. Zhang, X. Huang, H.Y. Wang, W.Z. Cai, R. Chen, J.J. Gao, X.F. Yang, W. Chen, Y.Q. Huang, H.M. Chen, C.M. Li, T. Zhang, B. Liu, Atomically dispersed Ni(i) as the active site for electrochemical CO_2 reduction, *Nat. Energy* 3 (2018) 140–147, <https://doi.org/10.1038/s41560-017-0078-8>.
- [48] B.T. Chen, B.R. Li, Z.Q. Tian, W.B. Liu, W.P. Liu, W.W. Sun, K. Wang, L. Chen, J. Z. Jiang, Enhancement of mass transfer for facilitating industrial-level CO_2 electroreduction on atomic Ni-N₄ sites, *Adv. Energy Mater.* 11 (2021), 2102152, <https://doi.org/10.1002/aenm.202102152>.
- [49] P.L. Lu, Y.J. Yang, J.N. Yao, M. Wang, S. Dipazir, M.L. Yuan, J.X. Zhang, X. Wang, Z.J. Xie, G.J. Zhang, Facile synthesis of single-nickel-atomic dispersed N-doped carbon framework for efficient electrochemical CO_2 reduction, *Appl. Catal. B Environ.* 241 (2019) 113–119, <https://doi.org/10.1016/j.apcatb.2018.09.025>.
- [50] D. Zhao, K. Yu, P.Y. Song, W.Y. Feng, B.T. Hu, W.C. Cheong, Z.W. Zhuang, S.J. Liu, K.A. Sun, J.T. Zhang, C. Chen, Atomic-level engineering $\text{Fe}_1\text{N}_2\text{O}_2$ interfacial structure derived from oxygen-abundant metal-organic frameworks to promote electrochemical CO_2 reduction, *Energy Environ. Sci.* 15 (2022) 3795–3804, <https://doi.org/10.1039/d2ee00878e>.
- [51] X.L. Zu, X.D. Li, W. Liu, Y.F. Sun, J.Q. Xu, T. Yao, W.S. Yan, S. Gao, C.M. Wang, S. Q. Wei, Y. Xie, Efficient and robust carbon dioxide electroreduction enabled by atomically dispersed Sn^{δ+} sites, *Adv. Mater.* 31 (2019), 1808135, <https://doi.org/10.1002/adma.201808135>.
- [52] H.S. Shang, T. Wang, J.J. Pei, Z.L. Jiang, D.N. Zhou, Y. Wang, H.J. Li, J.C. Dong, Z. B. Zhuang, W.X. Chen, D.S. Wang, J.T. Zhang, Y.D. Li, Design of a single-atom indium^{δ+}-N₄ interface for efficient electroreduction of CO_2 to formate, *Angew. Chem. Int. Ed.* 59 (2020) 22465–22469, <https://doi.org/10.1002/anie.202010903>.

- [53] X. Wang, F.L. Li, W.J. Yin, Y.B. Si, M. Miao, X.M. Wang, Y.Z. Fu, Atomically dispersed Sn modified with trace sulfur species derived from organosulfide complex for electroreduction of CO₂, *Appl. Catal. B Environ.* 304 (2022), 120936, <https://doi.org/10.1016/j.apcatb.2021.120936>.
- [54] D.D. Ma, S.G. Han, C.S. Cao, W.B. Wei, X.F. Li, B. Chen, X.T. Wu, Q.L. Zhu, Bifunctional single-molecular heterojunction enables completely selective CO₂-to-CO conversion integrated with oxidative 3D nano-polymerization, *Energy Environ. Sci.* 14 (2021) 1544–1552, <https://doi.org/10.1039/d0ee03731a>.
- [55] S.X. Ren, D. Joulie, D. Salvatore, K. Torbensen, M. Wang, M. Robert, C. P. Berlinguet, Molecular electrocatalysts can mediate fast, selective CO₂ reduction in a flow cell, *Science* 365 (2019) 367–369, <https://doi.org/10.1126/science.aax4608>.
- [56] Q.W. Chang, Y.M. Liu, J.H. Lee, D. Ologunagba, S. Hwang, Z.H. Xie, S. Kattel, J. H. Lee, J.G. Chen, Metal-coordinated phthalocyanines as platform molecules for understanding isolated metal sites in the electrochemical reduction of CO₂, *J. Am. Chem. Soc.* 144 (2022) 16131–16138, <https://doi.org/10.1021/jacs.2c06953>.
- [57] Y.R. Wang, Q. Huang, C.T. He, Y.F. Chen, J. Liu, F.C. Shen, Y.Q. Lan, Oriented electron transmission in polyoxometalate-metallocporphyrin organic framework for highly selective electroreduction of CO₂, *Nat. Commun.* 9 (2018) 4466, <https://doi.org/10.1038/s41467-018-06938-z>.
- [58] D.L. Meng, M.D. Zhang, D.H. Si, M.J. Mao, Y. Hou, Y.B. Huang, R. Cao, Highly selective tandem electroreduction of CO₂ to ethylene over atomically isolated nickel-nitrogen site/copper nanoparticle catalysts, *Angew. Chem. Int. Ed.* 60 (2021) 25485–25492, <https://doi.org/10.1002/anie.202111136>.
- [59] J. Wang, X. Huang, S.B. Xi, H. Xu, X. Wang, Axial modification of cobalt complexes on heterogeneous surface with enhanced electron transfer for carbon dioxide reduction, *Angew. Chem. Int. Ed.* 59 (2020) 19162–19167, <https://doi.org/10.1002/anie.202008759>.
- [60] Y. Guo, W.J. Shi, H.J. Yang, Q.F. He, Z.M. Zeng, J.Y. Ye, X.R. He, R.Y. Huang, C. Wang, W.B. Lin, Cooperative stabilization of the [pyridinium-CO₂-Co] adduct on a metal-organic layer enhances electrocatalytic CO₂ reduction, *J. Am. Chem. Soc.* 141 (2019) 17875–17883, <https://doi.org/10.1021/jacs.9b09227>.
- [61] X. Zhang, Z.S. Wu, X. Zhang, L.W. Li, Y.Y. Li, H.M. Xu, X.X. Li, X.L. Yu, Z.S. Zhang, Y.Y. Liang, H.L. Wang, Highly selective and active CO₂ reduction electro-catalysts based on cobalt phthalocyanine/carbon nanotube hybrid structures, *Nat. Commun.* 8 (2017) 14675, <https://doi.org/10.1038/ncomms14675>.
- [62] X. Zhang, Y. Wang, M. Gu, M.Y. Wang, Z.S. Zhang, W.Y. Pan, Z. Jiang, H.Z. Zheng, M. Lucero, H.L. Wang, G.E. Sterbinsky, Q. Ma, Y.G. Wang, Z.X. Feng, J. Li, H.J. Dai, Y.Y. Liang, Molecular engineering of dispersed nickel phthalocyanines on carbon nanotubes for selective CO₂ reduction, *Nat. Energy* 5 (2020) 684–692, <https://doi.org/10.1038/s41560-020-0667-9>.
- [63] Y.C. Deng, J. Zhao, S.F. Wang, R.R. Chen, J. Ding, H.J. Tsai, W.J. Zeng, S.F. Hung, W. Xu, J.H. Wang, F. Jaouen, X.N. Li, Y.Q. Huang, B. Liu, *Operando* spectroscopic analysis of axial oxygen-coordinated single-Sn-atom sites for electrochemical CO₂ reduction, *J. Am. Chem. Soc.* 145 (2023) 7242–7251, <https://doi.org/10.1021/jacs.2c12952>.
- [64] S. Acharjya, J.C. Chen, M.H. Zhu, C. Peng, Elucidating the reactivity and nature of active sites for tin phthalocyanine during CO₂ reduction, *Greenh. Gases* 11 (2021) 1191–1197, <https://doi.org/10.1002/ghg.2081>.
- [65] G. Abarca, M. Viera, C. Aliaga, J.F. Marco, W. Orellana, J.H. Zagal, F. Tasca, In search of the most active Mn4 catalyst for the oxygen reduction reaction. The case of perfluorinated Fe phthalocyanine, *J. Mater. Chem. A* 7 (2019) 24776–24783, <https://doi.org/10.1039/c9ta09125d>.
- [66] S. Yuan, J.Y. Peng, Y.R. Zhang, D.J. Zheng, S. Bagi, T. Wang, Y. Román-Leshkov, Y. Shao-Horn, Tuning the Catalytic Activity of Fe-Phthalocyanine-Based Catalysts for the Oxygen Reduction Reaction by Ligand Functionalization, *ACS Catal.* 12 (2022) 7278–7287, <https://doi.org/10.1021/acscatal.2c00184>.
- [67] H.M. Xu, S.B. Xi, J. Li, S.K. Liu, P. Lyu, W. Yu, T. Sun, D.C. Qi, Q. He, H. Xiao, M. Lin, J.S. Wu, J. Zhang, J. Lu, Chemical design and synthesis of superior single-atom electrocatalysts via *in situ* polymerization, *J. Mater. Chem. A* 8 (2020) 17683–17690, <https://doi.org/10.1039/d0ta05130f>.
- [68] K. Ye, Z.W. Zhou, J.Q. Shao, L. Lin, D.F. Gao, N. Ta, R. Si, G.X. Wang, X.H. Bao, In situ reconstruction of a hierarchical Sn-Cu/SnO_x core/shell catalyst for high-performance CO₂ electroreduction, *Angew. Chem. Int. Ed.* 59 (2020) 4814–4821, <https://doi.org/10.1002/anie.201916538>.
- [69] A. Zhang, Y.X. Liang, H.P. Li, S.L. Wang, Q.X. Chang, K.Y. Peng, Z.G. Geng, J. Zeng, Electronic tuning of SnS₂ nanosheets by hydrogen incorporation for efficient CO₂ electroreduction, *Nano Lett.* 21 (2021) 7789–7795, <https://doi.org/10.1021/acs.nanolett.1c02757>.
- [70] C.W. Dirk, T. Inabe, K.F. Schoch Jr., T.J. Marks, *J. Am. Chem. Soc.* 105 (1983) 1539–1550, <https://doi.org/10.1021/ja00344a022>.
- [71] Y.P. Liu, W.F. Sheng, Z.H. Wu, Synchrotron radiation and its applications progress in inorganic materials, *J. Inorg. Mater.* 36 (2021) 901–918, <https://doi.org/10.15541/jim20200703>.
- [72] J. Gu, C.S. Hsu, L.C. Bai, H.M. Chen, X.L. Hu, Atomically dispersed Fe³⁺ sites catalyze efficient CO₂ electroreduction to CO, *Science* 364 (2019) 1091–1094, <https://doi.org/10.1126/science.aaw7515>.
- [73] A. Rismanchian, Y.W. Chen, S.S.C. Chuang, *situ* infrared study of photoreaction of ethanol on Au and Ag/TiO₂, *Catal. Today* 264 (2016) 16–22, <https://doi.org/10.1016/j.cattod.2015.07.038>.
- [74] T. Chen, G.P. Wu, Z.C. Feng, G.S. Hu, W.G. Su, P.L. Ying, C. Li, *In situ* FT-IR study of photocatalytic decomposition of formic acid to hydrogen on Pt/TiO₂ catalyst, *Chin. J. Catal.* 29 (2008) 105–107, [https://doi.org/10.1016/s1872-2067\(08\)60019-4](https://doi.org/10.1016/s1872-2067(08)60019-4).